J. Plasma Phys. (2024), *vol*. 90, 905900509
Published by Cambridge University Press

doi:10.1017/S0022377824001223

Electron scattering on small-scale electrostatic fields in the shock front

Michael Gedalin †

Department of Physics, Ben-Gurion University of the Negev, 8410501 Beer-Sheva, Israel

(Received 29 June 2024; revised 5 September 2024; accepted 5 September 2024)

Electron heating and acceleration in collisionless shocks is a long-standing problem. Rapid isotropization of heated electrons cannot be explained solely by the cross-shock potential. In addition, the macroscopic cross-shock potential prevents efficient reflection and injection into the diffusive acceleration regime. Recent observations have shown that small-scale electric fields are present in the shock front, together with the large-scale cross-shock potential. These small-scale fields have been found also in the upstream and downstream regions. Electron heating in shocks is produced by the combined action of the large- and small-scale fields. The large-scale potential determines the energy transferred to the electrons. The small-scale electrostatic fields scatter electrons. Here we study the scattering of electrons on the typical waveforms, namely solitary bipolar spikes and wavepackets. The main effect is the generation of backstreaming electrons with large pitch angles. It is found that wavepackets are more efficient in electron reflection in the interaction of electrons both with a single spike and with multiple spikes.

Keywords: space plasma physics, astrophysical plasmas

1. Introduction

Collisionless shocks are some of the most ubiquitous nonlinear systems in space plasmas. The forthcoming discussion is limited to fast non-relativistic shocks in magnetized electron–ion plasmas, as are most heliospheric shocks observed so far and the shocks in supernova remnants. Other shocks, like relativistic unmagnetized Weibel-mediated shocks, are not within the scope of the present paper. In the shock frame, the mass, momentum and energy fluxes are conserved across the shock. When viewed in the shock frame, the energy of the directed flow of the incident plasma partly remains with the decelerated bulk flow, while the rest is redistributed to the heating of the bulk of ions and electrons and acceleration of a small number of charged particles to high energies. In fast magnetosonic shocks magnetic field enhancement also takes a part of the energy budget. The mechanism of ion heating is rather well understood (see e.g. Gedalin (2019) and references therein). Electron heating is typically substantially weaker and in strong shocks may constitute less than 10 % of the ion heating (Schwartz *et al.* 1988; Ghavamian *et al.* 2013; Gedalin *et al.* 2023). Yet, knowledge of the amount of electron heating and of

† Email address for correspondence: gedalin@bgu.ac.il

the physical mechanism of the formation of the heated electron distribution is crucial for understanding of the physics of remote astrophysical shocks, where heated and accelerated electrons are responsible for most of the observed electromagnetic radiation (Reynolds & Keohane 1999; Laming 2000; Helder, Vink & Bassa 2011; Vink 2012; Ghavamian *et al.* 2013; Vink *et al.* 2015). Heliospheric observations allow us to study the mechanisms of electron heating and acceleration with *in situ* measurements.

Electrons are efficiently heated in the shock front (Bame *et al.* 1979). The first explanations involved wave–particle heating due to current-driven instabilities (Galeev 1984). Later, the view changed to the dominant role of the macroscopic fields while the turbulence was suggested to be a result, not a cause, of the heating process (Feldman *et al.* 1982). Adiabatic magnetic compression (conservation of the magnetic moment) alone would result in perpendicular heating at the expense of the parallel degree of freedom. Here perpendicular and parallel refer to the direction of the local magnetic field. Transfer of energy from ions requires the existence of the cross-shock potential which decelerates ions and accelerates electrons across the shock. Let x be the coordinate along the shock normal of a planar shock, for simplicity. In what follows we frequently refer to two shock frames. The normal incidence frame (NIF) is the shock frame in which the upstream plasma flow is along the shock normal. The de Hoffman–Teller frame (HT) is the shock frame in which the upstream plasma flow is along the upstream magnetic field. In either of these, the cross-shock potential is $\phi = -\int E_x \,\mathrm{d}x$, where E_x is the electric field. In the HT there is no other macroscopic electric field, so each proton loses the same energy $e\phi_{\mathrm{HT}}$ upon crossing from upstream to downstream, and each electron gains the same energy. Adiabatic acceleration in a macroscopic cross-shock potential (Feldman *et al.* 1982; Goodrich & Scudder 1984; Scudder *et al.* 1986*b*; Thomsen *et al.* 1987; Schwartz *et al.* 1988; Hull *et al.* 2001) would result in acceleration of the bulk of electrons along the magnetic field, while an additional mechanism is required to isotropize the distribution. Liouville mappings in such a macroscopic cross-shock field (Scudder *et al.* 1986*a*; Hull *et al.* 2001) should be done in both directions since there is substantial leakage from the heated downstream electron distribution. Unless global demagnetization occurs in a very thin shock, inside the ramp the electron distribution should consist of two counter-streaming flows and be strongly unstable. The cross-shock potential issue evolved from a Gaussian fit to three points per transition (Scudder *et al.* 1986*b*) and ignoring higher-resolution measurements (Wygant, Bensadoun & Mozer 1987) to the suspicion that there is no macroscopic cross-shock potential at all, given the measurements of the strong small-scale fields. There is no contradiction though. The relation $\phi = -\int E_x \,\mathrm{d}x$ is valid even if E_x consists of large-amplitude small-scale bursts and a weak mean field slowly varying at the scale of the whole ramp. Direct measurements of the cross-shock potential are difficult (Bale *et al.* 2002; Balikhin *et al.* 2002; Walker *et al.* 2004; Dimmock *et al.* 2012; Hanson *et al.* 2019). Proper integration across the shock requires switching to the NIF or HT and is therefore sensitive to the determination of the shock normal and the shock speed. Both are prone to substantial errors (Gedalin, Russell & Dimmock 2021). Despite the problems of direct observational determination of the cross-shock potential, its existence is necessary to transfer energy from ions to electrons and magnetic field. It can be estimated by examination of the ion distributions at the shock front and by careful comparison of theoretical predictions with observations (Pope, Gedalin & Balikhin 2019; Gedalin *et al.* 2020).

Observations at the Earth bow shock, especially by the Magnetospheric Multiscale (MMS) Mission, clearly show that the shock transition is filled with small-scale coherent electrostatic structures which can be expected to affect electron heating and, possibly, electron reflection and injection into the pre-acceleration regime (Bale *et al.* 2002;

https://doi.org/10.1017/S0022377824001223 Published online by Cambridge University Press

Hull *et al.* 2006; Hobara *et al.* 2008; Wilson *et al.* 2010, 2014*a*,*b*; Goodrich *et al.* 2018; Vasko *et al.* 2018; Hanson *et al.* 2019; Vasko *et al.* 2020; Wang *et al.* 2020, 2021, 2022). The presence of large-amplitude small-scale electrostatic structures all over the shock led to the suspicion that they alone can decelerate ions (Goodrich *et al.* 2018). It was shown, however, that this does not happen (Gedalin 2020). Demagnetization of electrons in a strongly inhomogeneous electric field of the shock ramp was predicted by Balikhin, Gedalin & Petrukovich (1993). Similar demagnetization occurs in small-scale structures (see Cameron & Schwartz 2013; Mozer & Sundkvist 2013). Recent works revive the stochastic interaction of electrons with short-scale electrostatic fields as the major player in electron heating (Amano & Hoshino 2009; Matsumoto, Amano & Hoshino 2013; Artemyev *et al.* 2014; Matsumoto *et al.* 2015; Artemyev, Rankin & Vasko 2017; Katou & Amano 2019; Tran & Sironi 2020; Artemyev *et al.* 2022; Kamaletdinov *et al.* 2022), focusing on solitary bipolar structures, often of Debye size. At present, the two approaches to electron heating are often considered mutually exclusive. Electrons are thought to be heated by either macroscopic cross-shock potential or many small-scale electric structures. Gedalin (2020) proposed a combined approach taking into account both small-scale electrostatic structures and a large-scale potential. In this approach, the integrated cross-shock potential determines the energy transferred to the electrons while the small-scale fields provide scattering in the velocity space to shape the distribution.

Electron acceleration is less studied. Sufficiently high-energy electrons may be scattered by the ion-scale turbulence and, therefore, may be accelerated by the diffusive shock acceleration (Jebaraj *et al.* 2023). Such relativistic electrons have been detected at the Earth bow shock and interplanetary shocks (Liu, Angelopoulos & Lu 2019; Jebaraj *et al.* 2023). The problem is to convert some electrons from the thermal distribution into a superthermal tail which would be able to cross the shock back and forth and gradually gain more energy. This requires electron reflection, as a first step. Reflection by magnetic mirroring in nearly perpendicular shocks (Leroy & Mangeney 1984; Wu 1984), injection by whistlers (see e.g. Riquelme & Spitkovsky (2011) and references therein) or pre-acceleration due to trapping and drift in a rippled shock front (see Trotta & Burgess (2019) and references therein) have been proposed, all for high-Mach-number quasi-perpendicular shocks, typically $\theta_{Bn} > 80^\circ$. Here θ_{Bn} is the angle between the shock normal and the upstream magnetic field vector. The Alfvén Mach number is the ratio of the shock speed, that is, the upstream plasma velocity along the shock normal, V_u, to the Alfvén speed, $v_A = B_u/\sqrt{4\pi n_u m_p}$. Here B_u is the upstream magnetic field magnitude, n_u is the upstream ion number density and m_p is the proton mass. Low-Mach-number or quasi-parallel shocks are supposed to have substantially smaller gradients (Burgess & Scholer 2013; Krasnoselskikh *et al.* 2013), required for the mentioned mechanisms. Small-scale electrostatic fields may be able to reflect a part of the low-energy electrons, thus starting injection.

In this paper we study the effect of small-scale fields on the electron distributions, focusing on the difference of the effects produced by various waveforms.

2. Observations

At present, the MMS is widely regarded as the state of the art since MMS measures particles also at high resolution. The DC magnetic field and magnetic fluctuations are measured separately by different instruments. The DC component is measured by the FluxGate Magnetometer at a rate of 128 samples s^{-1} in the burst mode (Russell *et al.* 2016). The Search-Coil Magnetometer (SCM) measures magnetic waveforms which are provided at a rate of 8192 s s^{-1} (Le Contel *et al.* 2016). The Spin-plane Double Probes and Axial Double Probes provide the electric field vector (EDP) at a rate of 8192 s s^{-1} with nominal precision of $\sim$1 mV m^{-1} (Ergun *et al.* 2016; Lindqvist *et al.* 2016; Torbert

https://doi.org/10.1017/S0022377824001223 Published online by Cambridge University Press

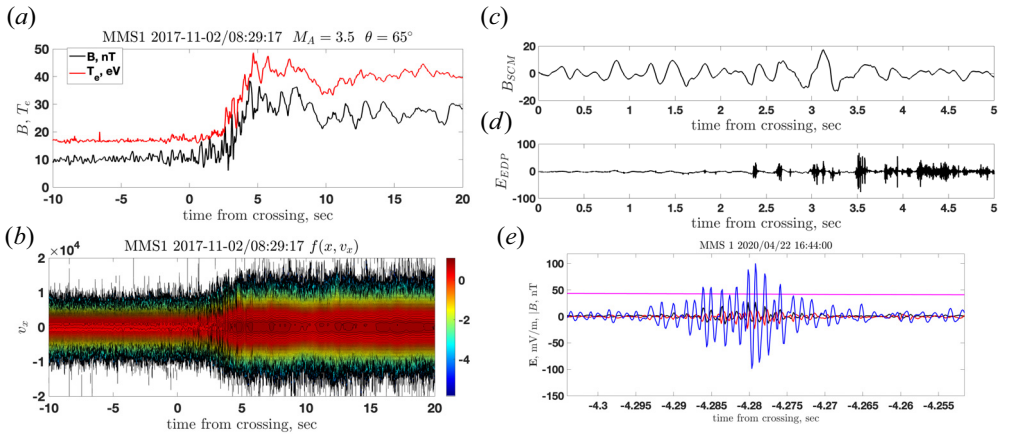

FIGURE 1. (*a*) The magnitude of the DC magnetic field and the electron temperature calculated from FPI burst mode distributions, at 30 ms cadence. (*b*) The reduced distribution function $f(x, v_x)$ obtained from the same FPI data. (*c*) One component of the SCM magnetic field measured at a rate of 8192 s s^{-1}. (*d*) One component of the EDP electric field measured at a rate of 8192 s s^{-1}. (*e*) The most abundant shape of the small-scale electric field.

et al. 2016). These electric field measurements include the DC component. Level 2 data are provided at the MMS Science Data Center https://lasp.colorado.edu/mms/sdc/public/. Electron distributions are measured by the Fast Plasma Instrument (FPI) at 30 ms cadence, in the burst mode (Pollock *et al.* 2016). Figure 1 illustrates the available measurements by MMS. Figure 1(*a*) shows the magnetic field and electron temperature in a moderate-Mach-number, M_A, quasi-perpendicular, $\theta_{Bn} = 65°$, terrestrial bow shock crossing by MMS1, chosen rather arbitrarily from the database developed by the SHARP collaboration (Lalti *et al.* 2022). The crossing occurred on 2017-11-02 at 08:29:17 UTC. Figure 1(*b–d*) belongs to the same crossing. Figure 1(*e*) is for the shock on 2020-04-22 at 16:44:00 UTC with $M_A \approx 16$ and $\theta_{Bn} = 55°$. The main shock transition, according to the DC magnetic field, lasts 5 s, $0 < t < 5$, and the increase of the electron temperature from the upstream value to the maximum occurs there (figure 1*a*), which means that electron heating is prompt and is determined by the fields there. Figure 1(*c*) shows that the whole shock transition is covered by a wavetrain of the AC magnetic field with a period of 1 s. Figure 1(*d*) shows that the electric field bursts are intermittent. A most abundant burst has the shape of a wavepacket of a duration of 20–30 ms and a period of 1 ms. Other typical electric waveforms are a unipolar/solitary spike or a bipolar spike, both of 1 ms duration (Goodrich *et al.* 2018; Vasko *et al.* 2018, 2020; Wang *et al.* 2020, 2021; Vasko *et al.* 2022). It has to be noted that conversion of the duration into spatial dependence requires thorough analysis of the wave properties. The magnetic and electric activity presented in figure 1 has been found in quasi-perpendicular and quasi-parallel shocks as well, from the lowest- to highest-Mach-number shocks in the SHARP database.

3. Interaction with a single spike

The focus of this study is the effect of a single spike shape on the distribution of electrons. We numerically solve the equations of motion of electrons:

$$\dot{\boldsymbol{v}} = -\frac{e}{m_e}\left(\boldsymbol{E} + \frac{1}{c}\boldsymbol{v} \times \boldsymbol{B}\right), \tag{3.1}$$

https://doi.org/10.1017/S0022377824001223 Published online by Cambridge University Press

$$\dot{\boldsymbol{r}} = \boldsymbol{v}, \quad \dot{X} \equiv \frac{\mathrm{d}X}{\mathrm{d}t}, \tag{3.2a,b}$$

where the magnetic field $\boldsymbol{B}$ is a background field and the electric field includes both the background field and the spike field. The typical scale of variation of the background fields is $\gtrsim c/\omega_{pi}$, where $\omega_{pi} = \sqrt{4\pi ne^2/m_p}$, while the spatial scale of a spike is substantially smaller than $c/\omega_{pe} = (m_e/m_p)^{1/2}(c/\omega_{pi})$. Therefore, the background fields are taken as constant. In particular, the background electric field is zero, so that initially, electrons flow along the local magnetic field $\boldsymbol{B} = B_0(\cos\theta, 0, \sin\theta)$. Note that θ is not necessarily the same as θ_{Bn}, that is, the coordinate x is not necessarily along the shock normal. We consider a spike as a planar stationary structure depending only on one coordinate $E_x = E_x(x)$. In this approach, the direction of the spike propagation with respect to the local magnetic field is θ; the direction of propagation with respect to the shock normal is not relevant. Three types of the small-scale electrostatic field E_x are modelled.

1. A unipolar spike is modelled as a Gaussian:

$$E_x = -\frac{\phi}{\sqrt{2\pi}L}\exp\left(-\frac{(x-x_c)^2}{2L^2}\right) \tag{3.3}$$

of width L and the centre at x_c. The potential across the shape is ϕ. Unipolar spikes were not found in the above observations but, in principle, the whole cross-shock potential might be made of a series of such spikes, and it is at least of theoretical interest to analyse the electron interaction of such a spike.

2. A bipolar spike is modelled as a difference of Gaussians given by (3.3):

$$E_x = -\frac{\phi_1}{\sqrt{2\pi}L_1}\exp\left(-\frac{(x-x_1)^2}{2L_1^2}\right) - \frac{\phi_2}{\sqrt{2\pi}L_2}\exp\left(-\frac{(x-x_2)^2}{2L_2^2}\right). \tag{3.4}$$

The centres of the Gaussians, x_1 and x_2, are shifted and the amplitudes ϕ_1 and ϕ_2 are of opposite signs. The total cross-spike potential is $\phi_1 + \phi_2$, while the maximum potential is $\approx \max(|\phi_1|, |\phi_2|)$.

3. A wavepacket is modelled using the expression

$$E_x = E_0\cos(2\pi x/W)\exp\left(-\frac{x^2}{2L^2}\right), \tag{3.5}$$

where W is the wavelength of the wavetrain and L is the width of the Gaussian envelope. The spatial scale of a single spike is much smaller than the spatial scale of the magnetic field variation and substantially smaller than the electron inertial length.

The initial electron distribution is taken as bi-Maxwellian:

$$f(v_\parallel, v_\perp) = \frac{1}{(2\pi)^{3/2}v_T^3}\exp\left(-\frac{(v_\parallel - V_d)^2}{2Av_T^2} - \frac{v_\perp^2}{2v_T^2}\right), \tag{3.6}$$

where $v_\parallel = \boldsymbol{v}\cdot\boldsymbol{B}/|\boldsymbol{B}|$, $v_\perp^2 = v^2 - v_\parallel^2$, V_d is the flow velocity along the magnetic field, $v_T^2 = T_\perp/m_e$ is the perpendicular thermal speed, $T_\perp$ is the perpendicular temperature and $A = T_\parallel/T_\perp$ is the anisotropy ratio, that is, the ratio of the parallel and perpendicular

https://doi.org/10.1017/S0022377824001223 Published online by Cambridge University Press

temperatures. The perpendicular electron thermal gyroradius is

$$\rho_e = \frac{v_{Te}}{\Omega_e} = \frac{m_e}{m_i}\sqrt{\frac{m_i}{m_e}}\frac{v_{Ti}}{\Omega_i} = \sqrt{\frac{m_e}{m_i}}\sqrt{\frac{\beta}{2}}\frac{v_A}{\Omega_i} = \frac{c}{\omega_{pe}}\sqrt{\frac{\beta_e}{2}}, \tag{3.7}$$

where $v_{Te} = \sqrt{T_e/m_e}$ is the electron thermal speed, $\Omega_e = eB/m_e c$ is the electron gyrofrequency, $\omega_{pe} = \sqrt{4\pi n_e e^2/m_e}$ is the electron plasma frequency, B and n are the local magnetic field magnitude and electron number density, respectively, and $\beta_e = 8\pi n T_e/B^2$. For anisotropic distributions $T_e = T_\perp$. We also define $V_d = V_u/\cos\theta$, that is, the incident electron flow velocity along the x direction is V_u, and $M = V_u/v_A$ is the Alfvénic Mach number of this flow. Note that all parameters defined above are local and not the shock parameters, e.g. the Mach number of the flow is not the shock Mach number. The parameter V_d is the drift velocity of the electrons measured in the spike frame and not in the shock frame.

It is convenient to normalize:

$$\boldsymbol{v}/V_u \to \boldsymbol{v}, \quad \boldsymbol{B}/B_u \to \boldsymbol{B}, \quad \boldsymbol{E}/(V_u B/c) \to \boldsymbol{E}, \tag{3.8a-c}$$

$$\Omega_e t \to t, \quad \omega_{pe}\boldsymbol{r}/c \to \boldsymbol{r}, \tag{3.9a,b}$$

which allows rewriting the equations of motion in the form

$$\dot{v}_x = -E_x + v_y \sin\theta, \tag{3.10}$$

$$\dot{v}_y = v_z \cos\theta - v_x \sin\theta, \tag{3.11}$$

$$\dot{v}_z = -v_y \sin\theta, \tag{3.12}$$

$$\dot{\boldsymbol{r}} = M\left(\frac{m_e}{m_p}\right)^{1/2}\boldsymbol{v}. \tag{3.13}$$

In all these spikes electrons are demagnetized and their motion is non-adiabatic. We start tracing with incident bi-Maxwellian distribution drifting towards the spike in the positive direction of the x axis. We follow electrons until they appear well behind the spike (downstream) or well ahead of the spike (backstreaming), and the distributions $f(v_\parallel, f_\perp)$ are derived in both regions. These distributions do not depend on what position the electrons are registered at. Since the fields depend only on x and do not depend on time, the electron number flux in the x direction should be conserved throughout, which is achieved by assigning the weight $|v_{0x}|$ to each electron. Here $\boldsymbol{v}_0$ is the initial velocity of an electron.

3.1. *A unipolar spike*

We start with a solitary unipolar spike with a small positive cross-spike potential. Figure 2 shows the electrostatic field and the cross-spike potential for the chosen spike. The spike parameters are: the width $L = 0.01(c/\omega_{pe})$ and the amplitude corresponding to $2.4\times10^{-3}(m_p V_u^2/2)$. Typical potentials within spikes are $\phi \lesssim 0.1T_e$ (Kamaletdinov *et al.* 2022). For typical $T_e \sim 10$ eV and $m_p V_u^2 \sim 1$ keV, one has $\phi/(m_p V_u^2/2) \sim 2\times10^{-3}$.

Figure 3 shows the electron distributions. There were 80 000 electrons in the initial bi-Maxwellian with $\beta_\perp = 0.3$ and $A = 3$. The tracing was done for $\theta_{Bn} = 60^\circ$ and $M = 6$. The high initial $\beta_\parallel = 0.9$ results in $v_{T\parallel}/V_d = \sqrt{A\beta_\perp/2}\cos\theta(m_p/m_e)^{1/2}/M \approx 0.4$ which means that a significant fraction of the electrons in the initial bi-Maxwellian distribution move initially in the negative direction of the x axis and do not encounter the spike.

https://doi.org/10.1017/S0022377824001223 Published online by Cambridge University Press

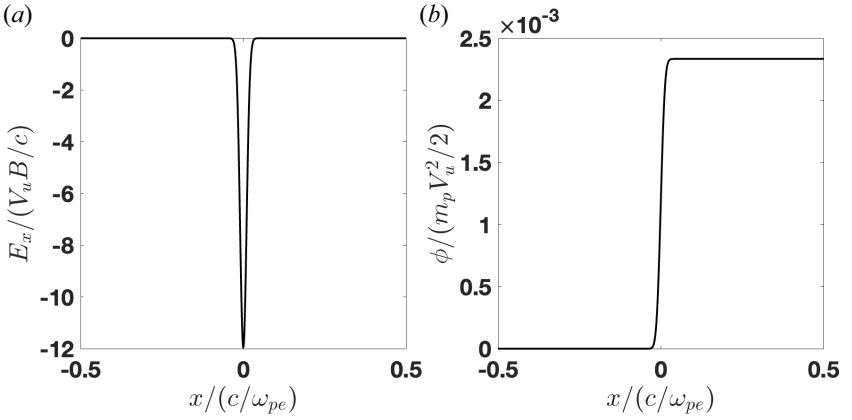

FIGURE 2. (*a*) The electrostatic field of the unipolar spike used for electron tracing. (*b*) The corresponding cross-spike potential.

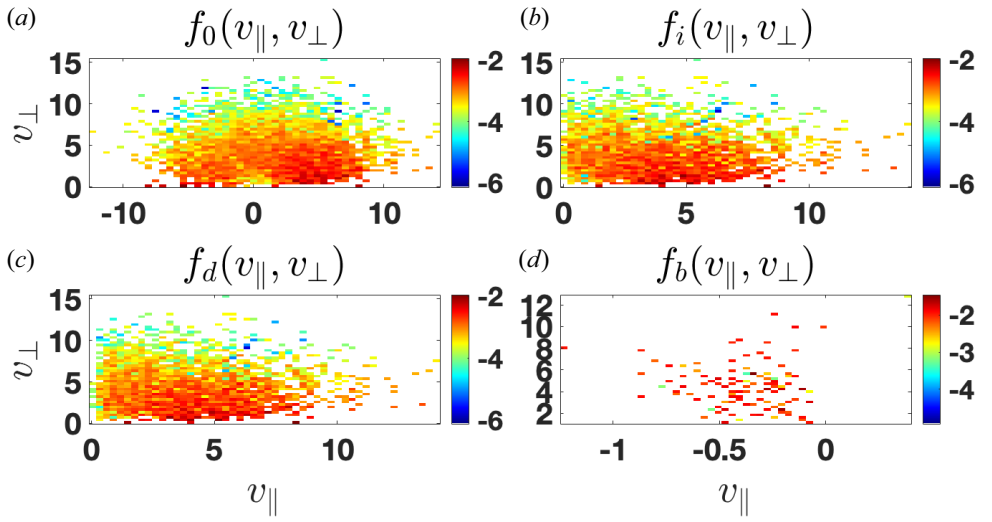

FIGURE 3. Interaction with the unipolar spike. (*a*) The initial bi-Maxwellian. (*b*) Only the incident electrons moving towards the spike. (*c*) The electrons crossing the spike and proceeding further downstream. (*d*) No backstreaming electrons reflected off the spike into the upstream region.

These electrons are excluded from the analysis. The bi-Maxwellian distribution $f_0(v_\parallel, v_\perp)$ is shown in figure 3(*a*), while the distribution of the forward (towards the spike) moving electrons $f_i(v_\parallel, v_\perp)$ is shown in figure 3(*b*). Figure 3(*c*) shows the distribution $f_d(v_\parallel, v_\perp)$ of the electrons that crossed the spike and proceeded further downstream without return. Figure 3(*d*) (empty in this case) is for the distribution $f_b(v_\parallel, v_\perp)$ of the ions that were reflected off the spike back to the upstream region and proceed further upstream without return. Of the total initial 80 000 particles 66 % encountered the spike and crossed it. We characterize the effect of the spike using the following parameters:

$$v_l = \left\langle \frac{v_\parallel}{V_u} \right\rangle, \quad T_l = \left\langle \frac{(v_\parallel - v_l)^2}{V_u^2} \right\rangle, \quad T_\perp = \frac{1}{2}\left\langle \frac{v_\perp^2}{V_u^2} \right\rangle. \tag{3.14a-c}$$

https://doi.org/10.1017/S0022377824001223 Published online by Cambridge University Press

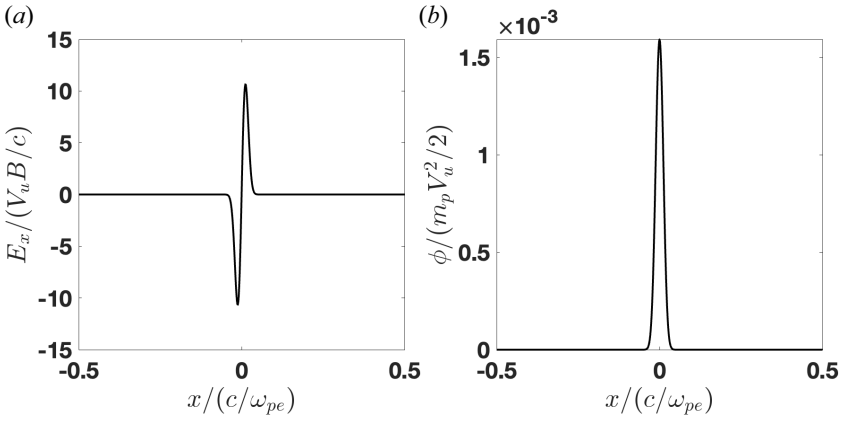

FIGURE 4. (*a*) The electrostatic field of the bipolar spike used for electron tracing. (*b*) The corresponding cross-spike potential.

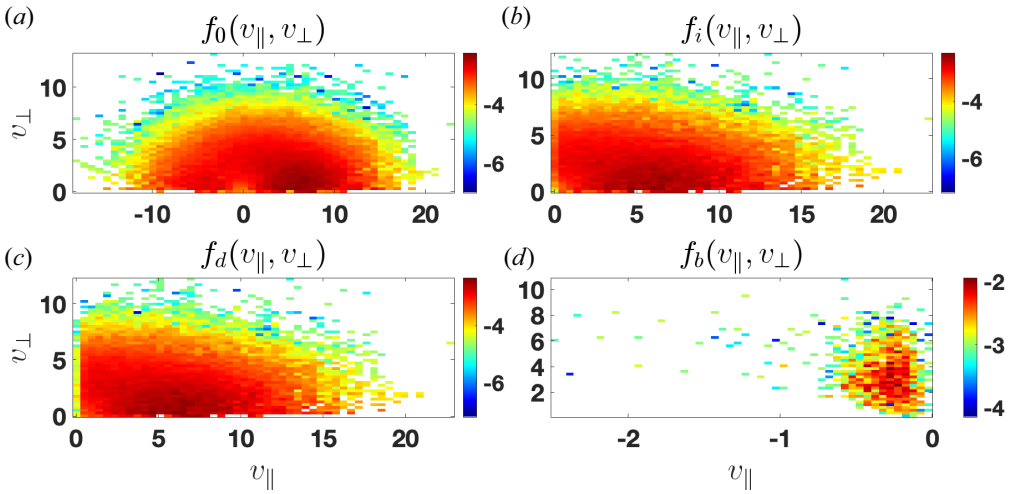

FIGURE 5. Interaction with the bipolar spike. (*a*) The initial bi-Maxwellian. (*b*) Only the incident electrons moving towards the spike. (*c*) The electrons crossing the spike and proceeding further downstream. (*d*) The backstreaming electrons reflected off the spike into the upstream region.

The averaging $\langle \cdots \rangle$ is calculated with each of the four distribution functions mentioned above. For the chosen parameters θ, M, β and A one has $v_{0l} = 1/\cos\theta \approx 1.97$, $T_{0l} \approx 22.7$, $T_{0p} = T_{0l}/3 \approx 7.6$, $v_{il} \approx 4.6$, $T_{il} \approx 10.5$ and $T_{ip} \approx 7.6$. For the downstream distribution $v_{dl} \approx 5.25$, $T_{dl} \approx 8.4$ and $T_{dp} \approx 7.75$. Thus, the electrons are accelerated across the spike, cooled in the parallel direction and slightly heated in the perpendicular direction. This means that the anisotropy ratio T_l/T_p decreases.

Next, we consider a bipolar spike which consists of the previous unipolar spike and its opposite with a shift of $0.02(c/\omega_{pe})$ between the centres. Figure 4 shows the electrostatic field and the cross-spike potential for the chosen bipolar spike. The potential reaches its maximum between the Gaussians but the overall potential is zero. The distributions are shown in figure 5. In this case, about 2 % of the incident electrons are returned to the

https://doi.org/10.1017/S0022377824001223 Published online by Cambridge University Press

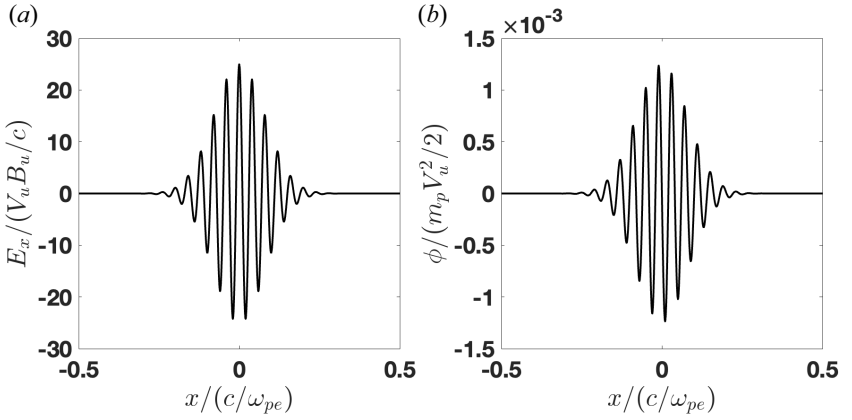

FIGURE 6. (*a*) The electrostatic field of the wavepacket used for electron tracing. (*b*) The corresponding cross-spike potential.

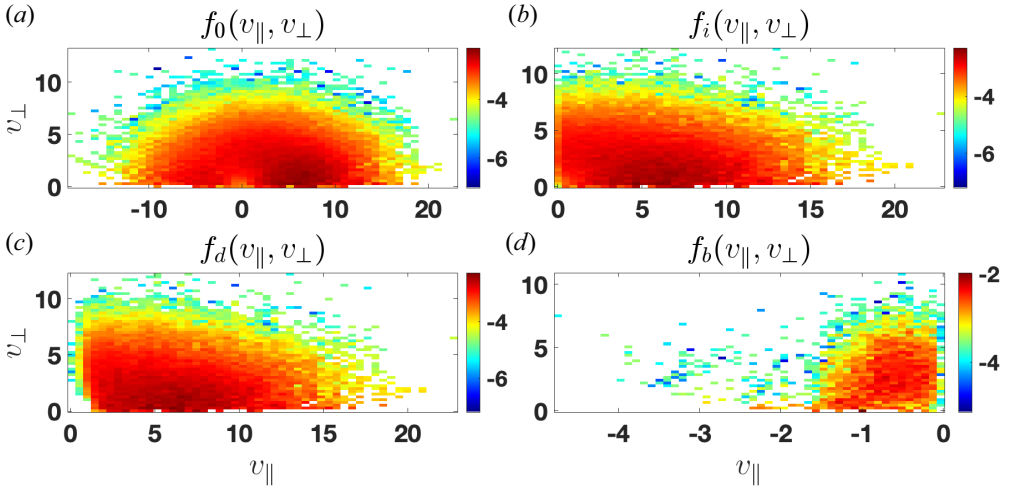

FIGURE 7. Interaction with the wavepacket. (*a*) The initial bi-Maxwellian. (*b*) Only the incident electrons moving towards the spike. (*c*) The electrons crossing the spike and proceeding further downstream. (*d*) The backstreaming electrons reflected off the spike and proceeding into the upstream region.

upstream region and stream backward. The corresponding parameters are $v_{dl} \approx 4.7$, $T_{dl} \approx 10$, $T_{dp} \approx 7.6$, $v_{bl} \approx -0.3$, $T_{bl} \approx 0.05$ and $T_{bp} \approx 7.9$. No acceleration of the downstream electrons occurs, and the temperatures are almost the same as for the forward-moving incident electron distribution.

Finally, we analyse the interaction of the same incident electron distribution with the wavepacket shown in figure 6. The wavelength is $0.04(c/\omega_{pe})$ and the width of the Gaussian envelope is $0.08(c/\omega_{pe})$. The maximum potential is $1.2 \times 10^{-3}(m_p V_u^2/2)$. About 12 % of the incident electrons are reflected. The corresponding distributions are shown in figure 7. The parameters of the downstream and backstreaming electrons are $v_{dl} \approx 5.2$, $T_{dl} \approx 9.3$, $T_{dp} \approx 7.8$, $v_{bl} \approx -0.7$, $T_{bl} \approx 0.22$ and $T_{bp} \approx 6.5$.

https://doi.org/10.1017/S0022377824001223 Published online by Cambridge University Press

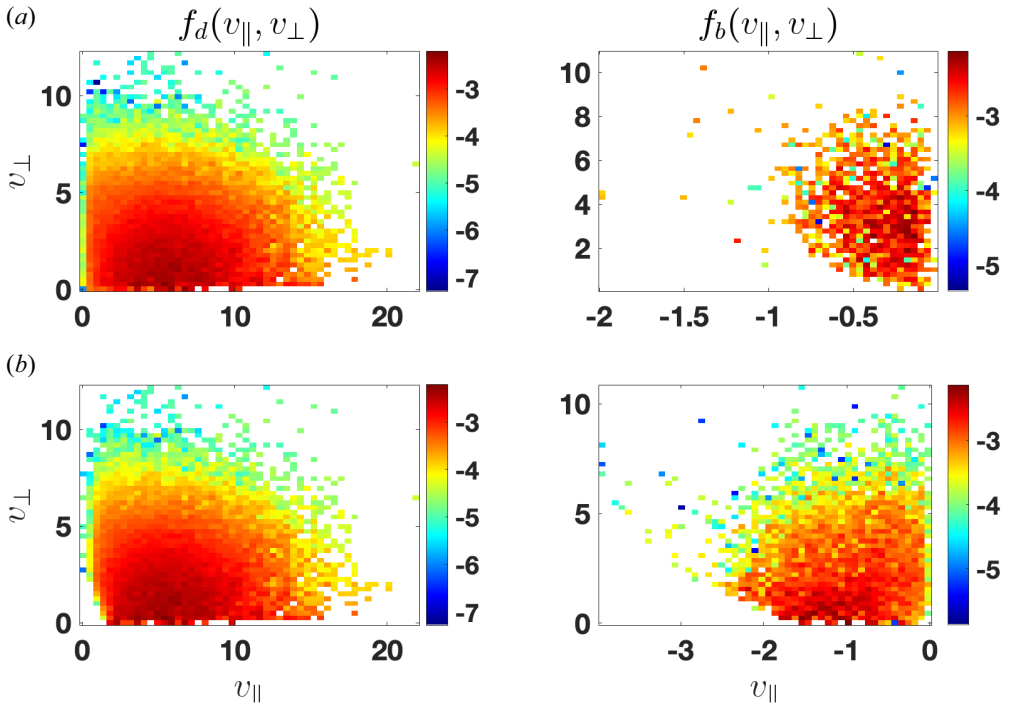

FIGURE 8. The downstream and backstreaming electron distributions for $\theta = 30^\circ$. (a) The interaction with the bipolar structure. (b) The interaction with the wavepacket.

In all three types of spikes, the maximal potentials are similar. All three are capable of reflecting electrons, the wavepacket being the most efficient. The backstreaming electrons have perpendicular temperatures substantially higher than parallel temperatures.

To understand the dependence on the shock angle, electron tracing was performed for the above bipolar structure and wavepacket and $\theta_{Bn} = 30^\circ$. Figure 8 shows the downstream and backstreaming electron distributions for $\theta = 30^\circ$. The main effect is the increase of the fraction of backstreaming ions: 3 % for the bipolar structure and 15 % for the wavepacket.

4. Interaction with multiple spikes

The shock front is filled with a large number of spikes, and the electron distribution is eventually formed due to interaction with many small-scale structures, as well as the mean electric field and the inhomogeneous magnetic field. The roles of the large-scale and small-scale electric fields have been elucidated in a simple model (Gedalin 2020) showing that the total energetics is related to the overall cross-shock potential while the small-scale fields shape the electron distribution. The details of the effect of the spikes should be the subject of a separate study. Here we analyse the interaction of electrons with several spikes in a row, at the spatial scale where the magnetic field variations may be neglected. Figure 9 shows the electric field and the potential of 10 consecutive identical bipolar spikes and the downstream and backstreaming electron distributions for $\theta = 60^\circ$ and the same $M = 6$, $\beta_\perp = 0.3$ and $A = 3$ as above.

Figure 10 shows the electric field and the potential of 10 consecutive identical wavepackets, as well as the downstream and backstreaming electron distributions for $\theta = 60^\circ$ and the same $M = 6$, $\beta_\perp = 0.3$ and $A = 3$ as above. The main effect of multiple

https://doi.org/10.1017/S0022377824001223 Published online by Cambridge University Press

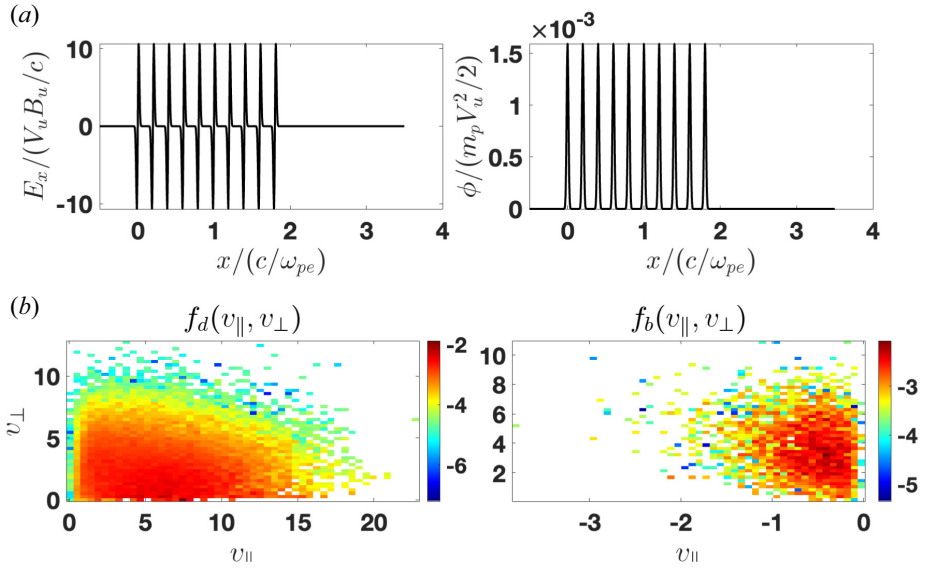

FIGURE 9. (*a*) The electric field and the potential of 10 consecutive bipolar spikes. (*b*) The downstream and backstreaming electron distributions for $\theta = 60°$.

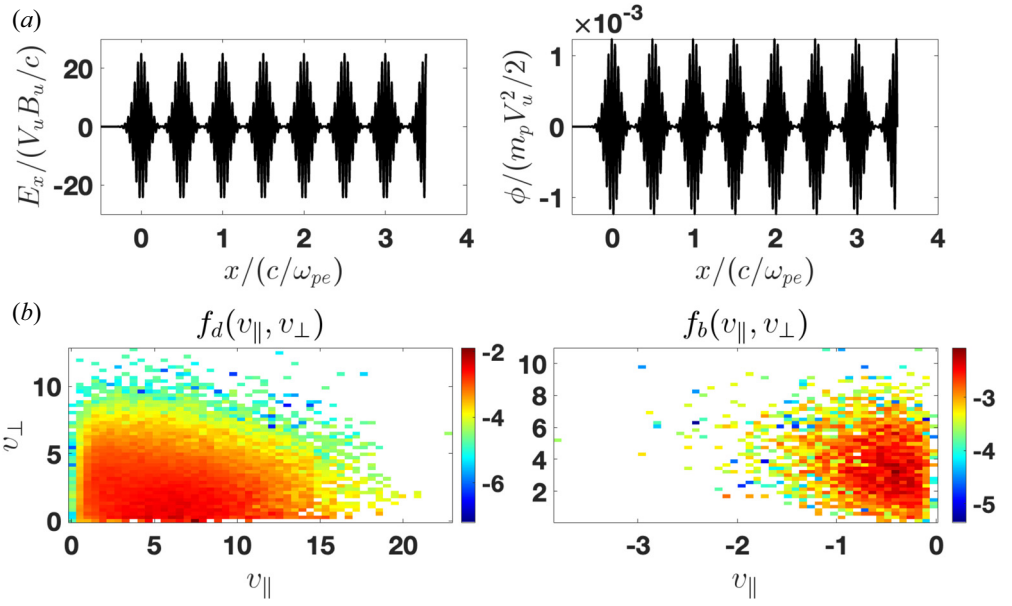

FIGURE 10. (*a*) The electric field and the potential of 10 consecutive wavepackets. (*b*) The downstream and backstreaming electron distributions for $\theta = 60°$.

encounters with spikes is the enhancement of reflection: about 7 % of backstreaming ions for the multiple bipolar structures and about 22 % for the multiple wavepackets.

It is of interest to check what would happen if a mean electric field were present also. Figure 11 shows the electric field and the potential of 10 consecutive identical wavepackets and a superimposed large-scale electric field, together with the downstream

https://doi.org/10.1017/S0022377824001223 Published online by Cambridge University Press

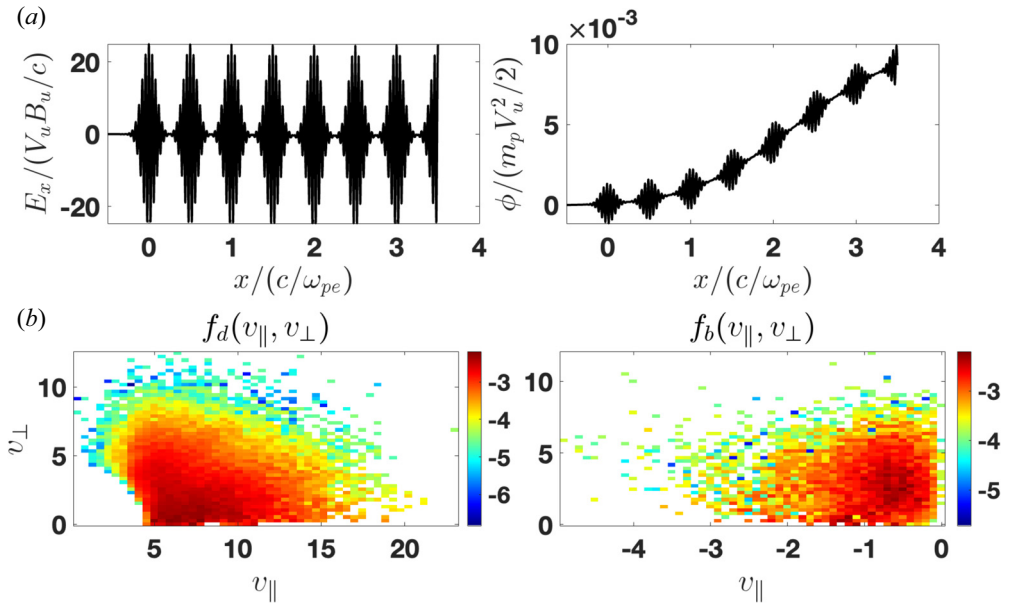

FIGURE 11. (*a*) The electric field and the potential of 10 consecutive wavepackets and a superimposed large-scale electric field (only a part is shown). (*b*) The downstream and backstreaming electron distributions.

and backstreaming electron distributions for $\theta = 60^\circ$ and the same $M = 6$, $\beta_\perp = 0.3$ and $A = 3$ as above. The large-scale field is modelled as follows:

$$E_x = E_0 \exp\left(-\frac{(x - x_0)^2}{2w_0^2}\right), \tag{4.1}$$

where $E_0 = -0.5(V_uB/c)$, $w_0 = c/\omega_{pe}$ and x_0 is in the middle of the region filled with the spikes. As would be expected, the mean electric field, which accelerates electrons across the spikes downstream, reduces the fraction of backstreaming electrons from 22 % without the field to 14 % with the field.

Finally, figure 12 shows the effect of the fields in figure 11 on the electron dynamics when the initial distribution is anisotropic with $A = 0.3$. There is no significant difference compared with the case of $A = 3$. In particular, the fraction of backstreaming electrons only slightly increases to 24 %.

5. Discussion and conclusions

The present study found that the main types of observed small-scale large-amplitude electrostatic structures in the shock front are solitary bipolar spikes and wavepackets. To understand the effect of these structures on the electron dynamics and the produced electron distributions, the structures have been modelled analytically, and test particle analyses have been performed with the incident bi-Maxwellian electrons. Interaction with a single structure and multiple structures has been studied. The spatial scale of the structure is much smaller than the scale of the magnetic field variation, which allowed us to simplify the analysis using the constant background magnetic field in the model. Since the electron thermal speed is substantially larger than the upstream plasma velocity and substantially larger than the speed of the electrostatic structure, it was possible to analyse the interaction

https://doi.org/10.1017/S0022377824001223 Published online by Cambridge University Press

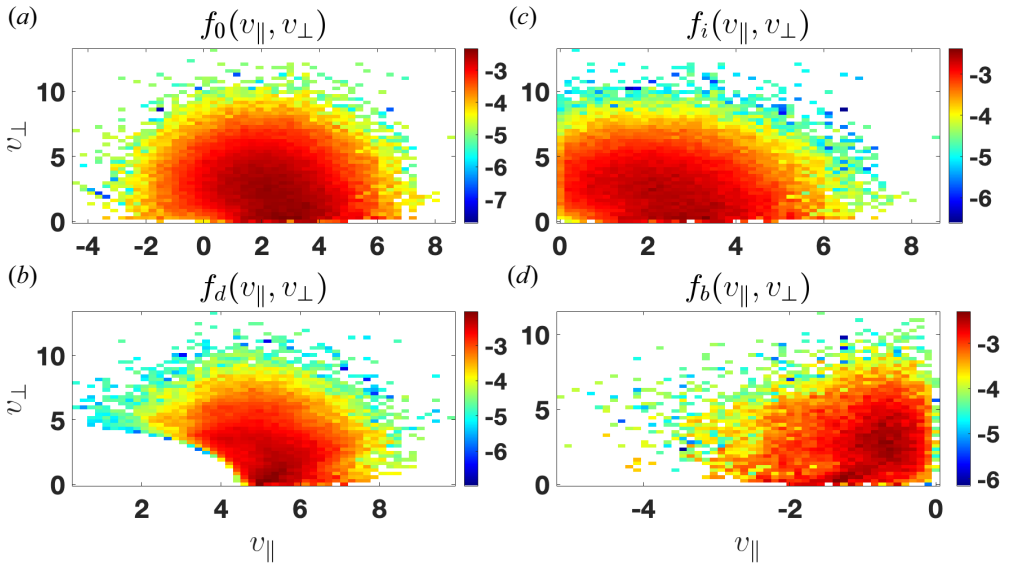

FIGURE 12. (*a*) The initial bi-Maxwellian. (*b*) Only the incident electrons moving towards the spike. (*c*) The electrons crossing the spike and proceeding further downstream. (*d*) The backstreaming electrons reflected off the spike into the upstream region.

in the frame of reference of the structure, with an oblique geometry of the magnetic field and initial flow of electrons along the magnetic field.

It is clear that the presented test particle analyses are limited, and the quantitative results cannot be compared directly with the observed shocks. Only one set of parameters has been treated here. In particular, a more comprehensive analysis should take into account the interaction with multiple spikes of different amplitudes propagating at different angles to the magnetic field, and with different speeds. Yet, qualitatively the interaction of an incident electron distribution with a spike will remain like the one considered here. The above analysis has shown that the main result of this interaction is electron reflection off a spike. The wavepackets appear to be the most efficient generators of backstreaming electrons, even in the presence of a large-scale mean electric field that drags electrons across the spike. The backstreaming particles have a larger spread of perpendicular velocities than of parallel velocities, and thus their pitch angles are effectively larger. The result of the interaction with multiple spikes does not differ qualitatively from the interaction with a single spike, but the reflection is stronger.

Acknowledgements

The work was partially supported by the European Union's Horizon 2020 research and innovation programme under grant agreement no. 101004131 (SHARP) and by the International Space Science Institute (ISSI) in Bern through International Team project no. 23-575.

Editor Antoine C. Bret thanks the referees for their advice in evaluating this article.

Declaration of interests

The author reports no conflict of interest.

https://doi.org/10.1017/S0022377824001223 Published online by Cambridge University Press

REFERENCES

AMANO, T. & HOSHINO, M. 2009 Electron shock surfing acceleration in multidimensions: two-dimensional particle-in-cell simulation of collisionless perpendicular shock. *Astrophys. J.* **690**, 244.

ARTEMYEV, A.V., RANKIN, R. & VASKO, I.Y. 2017 Nonlinear Landau resonance with localized wave pulses. *J. Geophys. Res.* **122**, 5519–5527.

ARTEMYEV, A.V., SHI, X., LIU, T.Z., ZHANG, X.-J., VASKO, I. & ANGELOPOULOS, V. 2022 Electron resonant interaction with whistler waves around foreshock transients and the bow shock behind the terminator. *J. Geophys. Res.* **127**.

ARTEMYEV, A.V., VASILIEV, A.A., MOURENAS, D., AGAPITOV, O.V. & KRASNOSELSKIKH, V.V. 2014 Electron scattering and nonlinear trapping by oblique whistler waves: the critical wave intensity for nonlinear effects. *Phys. Plasmas* **21**, 102903.

BALE, S.D., BALIKHIN, M.A., HORBURY, T.S., KRASNOSELSKIKH, V.V., KUCHAREK, H., MÖBIUS, E., WALKER, S.N., BALOGH, A., BURGESS, D., LEMBÈGE, B., *et al.* 2005 Quasi-perpendicular shock structure and processes. *Space Sci. Rev.* **118**, 161–203.

BALE, S.D., HULL, A., LARSON, D.E., LIN, R.P., MUSCHIETTI, L., KELLOGG, P.J., GOETZ, K. & MONSON, S.J. 2002 Electrostatic turbulence and debye-scale structures associated with electron thermalization at collisionless shocks. *Astrophys. J.* **575**, L25–L28.

BALIKHIN, M., GEDALIN, M. & PETRUKOVICH, A. 1993 New mechanism for electron heating in shocks. *Phys. Rev. Lett.* **70**, 1259–1262.

BALIKHIN, M.A., NOZDRACHEV, M., DUNLOP, M., KRASNOSELSKIKH, V., WALKER, S.N., ALLEYNE, H.S.T.C.K., FORMISANO, V., ANDRÉ, M., BALOGH, A., ERIKSSON, A., *et al.* 2002 Observation of the terrestrial bow shock in quasi-electrostatic subshock regime. *J. Geophys. Res.* **107**, 1155–SSH 1–9.

BAME, S.J., ASBRIDGE, J.R., GOSLING, J.T., HALBIG, M., PASCHMANN, G., SCKOPKE, N. & ROSENBAUER, H. 1979 High temporal resolution observations of electron heating at the bow shock. *Space Sci. Rev.* **23**, 75.

BURGESS, D., LUCEK, E.A., SCHOLER, M., BALE, S.D., BALIKHIN, M.A., BALOGH, A., HORBURY, T.S., KRASNOSELSKIKH, V.V., KUCHAREK, H., LEMBÈGE, B., *et al.* 2005 Quasi-parallel shock structure and processes. *Space Sci. Rev.* **118**, 205–222.

BURGESS, D. & SCHOLER, M. 2013 Microphysics of quasi-parallel shocks in collisionless plasmas. *Space Sci. Rev.* **178**, 513–533.

DIMMOCK, A.P., BALIKHIN, M.A., KRASNOSELSKIKH, V.V., WALKER, S.N., BALE, S.D. & HOBARA, Y. 2012 A statistical study of the cross-shock electric potential at low Mach number, quasi-perpendicular bow shock crossings using cluster data. *J. Geophys. Res.* **117**, 02210.

ERGUN, R.E., TUCKER, S., WESTFALL, J., GOODRICH, K.A., MALASPINA, D.M., SUMMERS, D., WALLACE, J., KARLSSON, M., MACK, J., BRENNAN, N., *et al.* 2016 The axial double probe and fields signal processing for the MMS mission. *Space Sci. Rev.* **199**, 167–188.

FELDMAN, W., BAME, S., GARY, S., GOSLING, J., MCCOMAS, D., THOMSEN, M., PASCHMANN, G., SCKOPKE, N., HOPPE, M. & RUSSELL, C. 1982 Electron heating within the earth's bow shock. *Phys. Rev. Lett.* **49**, 199.

GALEEV, A.A. 1984 The heating and acceleration of electrons by shocks. *Adv. Space Res.* **4**, 255.

GEDALIN, M. 2019 How non-stationary are moderately supercritical shocks? *J. Plasma Phys.* **85**, 905850505.

GEDALIN, M. 2020 Large-scale versus Small-scale fields in the shock front: effect on the particle motion. *Astrophys. J.* **895**, 59.

GEDALIN, M., GOLAN, M., VINK, J., GANUSHKINA, N. & BALIKHIN, M. 2023 Electron heating in shocks: statistics and comparison. *J. Geophys. Res.* **128**, e2023JA031627.

GEDALIN, M., RUSSELL, C.T. & DIMMOCK, A.P. 2021 Shock Mach number estimates using incomplete measurements. *J. Geophys. Res.* **126**, e2021JA029519.

GEDALIN, M., ZHOU, X., RUSSELL, C.T. & ANGELOPOULOS, V. 2020 Overshoot dependence on the cross-shock potential. *Ann. Geophys.* **38**, 17–26.

GHAVAMIAN, P., SCHWARTZ, S.J., MITCHELL, J., MASTERS, A. & LAMING, J.M. 2013 Electron-ion temperature equilibration in collisionless shocks: the supernova remnant-solar wind connection. *Space Sci. Rev*. **178**, 633–663.

GOODRICH, C.C. & SCUDDER, J.D. 1984 The adiabatic energy change of plasma electrons and the frame dependence of the cross-shock potential at collisionless magnetosonic shock waves. *J. Geophys. Res*. **89**, 6654–6662.

GOODRICH, K.A., ERGUN, R., SCHWARTZ, S.J., WILSON, L.B., NEWMAN, D., WILDER, F.D., HOLMES, J., JOHLANDER, A., BURCH, J., TORBERT, R., *et al.* 2018 MMS observations of electrostatic waves in an oblique shock crossing. *J. Geophys. Res*. **123**, 9430–9442.

HANSON, E.L.M., AGAPITOV, O.V., MOZER, F.S., KRASNOSELSKIKH, V., BALE, S.D., AVANOV, L., KHOTYAINTSEV, Y. & GILES, B. 2019 Cross-shock potential in rippled versus planar quasi-perpendicular shocks observed by MMS. *Geophys. Res. Lett*. **46**, 2381–2389.

HELDER, E.A., VINK, J. & BASSA, C.G. 2011 Temperature equilibration behind the shock front: an optical and X-ray study of RCW 86. *Astrophys. J*. **737**, 85.

HOBARA, Y., WALKER, S.N., BALIKHIN, M., POKHOTELOV, O.A., GEDALIN, M., KRASNOSELSKIKH, V., HAYAKAWA, M., ANDRÉ, M., DUNLOP, M., RÈME, H., *et al.* 2008 Cluster observations of electrostatic solitary waves near the Earth's bow shock. *J. Geophys. Res*. **113**, 05211.

HULL, A.J., LARSON, D.E., WILBER, M., SCUDDER, J.D., MOZER, F.S., RUSSELL, C.T. & BALE, S.D. 2006 Large-amplitude electrostatic waves associated with magnetic ramp substructure at Earth's bow shock. *Geophys. Res. Lett*. **33**, 5987.

HULL, A.J., SCUDDER, J.D., LARSON, D.E. & LIN, R. 2001 Electron heating and phase space signatures at supercritical, fast mode shocks. *J. Geophys. Res*. **106**, 15711–15733.

JEBARAJ, C.I., DRESING, N., KRASNOSELSKIKH, V., AGAPITOV, O.V., GIESELER, J., TROTTA, D., WIJSEN, N., LAROSA, A., KOULOUMVAKOS, A., PALMROOS, C., *et al.* 2023 Relativistic electron beams accelerated by an interplanetary shock. *Astron. Astrophys*. **680**, L7.

KAMALETDINOV, S.R., VASKO, I.Y., ARTEMYEV, A.V., WANG, R. & MOZER, F.S. 2022 Quantifying electron scattering by electrostatic solitary waves in the Earth's bow shock. *Phys. Plasmas* **29**, 082301.

KATOU, T. & AMANO, T. 2019 Theory of stochastic shock drift acceleration for electrons in the shock transition region. *Astrophys. J*. **874**, 119.

KENNEL, C.F. 1988 Shock structure in classical magnetohydrodynamics. *J. Geophys. Res*. **93**, 8545–8557.

KRASNOSELSKIKH, V., BALIKHIN, M., WALKER, S.N., SCHWARTZ, S., SUNDKVIST, D., LOBZIN, V., GEDALIN, M., BALE, S.D., MOZER, F., SOUCEK, J., *et al.* 2013 The dynamic quasiperpendicular shock: cluster discoveries. *Space Sci. Rev*. **178**, 535–598.

LALTI, A., KHOTYAINTSEV, Y.V., DIMMOCK, A.P., JOHLANDER, A., GRAHAM, D.B. & OLSHEVSKY, V. 2022 A database of MMS bow shock crossings compiled using machine learning. *J. Geophys. Res*. **127**.

LAMING, J. 2000 Electron heating at SNR collisionless shocks. *Astrophys. J. Suppl*. **127**, 409.

LE CONTEL, O., LEROY, P., ROUX, A., COILLOT, C., ALISON, D., BOUABDELLAH, A., MIRIONI, L., MESLIER, L., GALIC, A., VASSAL, M.C., *et al.* 2016 The search-coil magnetometer for MMS. *Space Sci. Rev*. **199**, 257–282.

LEROY, M.M. & MANGENEY, A. 1984 A theory of energization of solar wind electrons by the earth's bow shock. *Ann. Geophys*. **2**, 449–456.

LINDQVIST, P.-A., OLSSON, G., TORBERT, R.B., KING, B., GRANOFF, M., RAU, D., NEEDELL, G., TURCO, S., DORS, I., BECKMAN, P., *et al.* 2016 The spin-plane double probe electric field instrument for MMS. *Sp. Sci. Rev*. **199**, 137–165.

LIU, T.Z., ANGELOPOULOS, V. & LU, S. 2019 Relativistic electrons generated at Earth's quasi-parallel bow shock. *Sci. Adv*. **5**, eaaw1368.

MATSUMOTO, Y., AMANO, T. & HOSHINO, M. 2013 Electron acceleration in a nonrelativistic shock with very high Alfvén Mach number. *Phys. Rev. Lett*. **111**, 215003.

MATSUMOTO, Y., AMANO, T., KATO, T.N. & HOSHINO, M. 2015 Stochastic electron acceleration during spontaneous turbulent reconnection in a strong shock wave. *Science* **347**, 974–978.

MOZER, F.S. & SUNDKVIST, D. 2013 Electron demagnetization and heating in quasi-perpendicular shocks. *J. Geophys. Res*. **118**, 5415–5420.

https://doi.org/10.1017/S0022377824001223 Published online by Cambridge University Press

POLLOCK, C., MOORE, T., JACQUES, A., BURCH, J., GLIESE, U., OMOTO, T., AVANOV, L., BARRIE, A., COFFEY, V., DORELLI, J., *et al.* 2016 Fast plasma investigation for magnetospheric multiscale. *Space Sci. Rev*. **199**, 331–406.

POPE, S.A., GEDALIN, M. & BALIKHIN, M.A. 2019 The first direct observational confirmation of kinematic collisionless relaxation in very low Mach number shocks near the earth. *J. Geophys. Res*. **165**, 3–15.

REYNOLDS, S. & KEOHANE, J. 1999 Maximum energies of shock-accelerated electrons in young shell supernova remnants. *Astrophys. J*. **525**, 368.

RIQUELME, M.A. & SPITKOVSKY, A. 2011 Electron injection by whistler waves in non-relativistic shocks. *Astrophys. J*. **733**, 63.

RUSSELL, C.T., ANDERSON, B.J., BAUMJOHANN, W., BROMUND, K.R., DEARBORN, D., FISCHER, D., LE, G., LEINWEBER, H.K., LENEMAN, D., MAGNES, W., *et al.* 2016 The Magnetospheric Multiscale Magnetometers. *Space Sci. Rev*. **199**, 189–256.

SCHWARTZ, S.J., THOMSEN, M.F., BAME, S.J. & STANSBERRY, J. 1988 Electron heating and the potential jump across fast mode shocks. *J. Geophys. Res*. **93**, 12923–12931.

SCUDDER, J., MANGENEY, A., LACOMBE, C., HARVEY, C., WU, C.S. & ANDERSON, R.R. 1986*a* The resolved layer of a collisionless, high beta, supercritical, quasi-perpendicular shock wave. III. Vlasov electrodynamics. *J. Geophys. Res*. **91**, 11075.

SCUDDER, J.D., AGGSON, T., AGGSON, T.L., MANGENEY, A., LACOMBE, C. & HARVEY, C.C. 1986*b* The resolved layer of a collisionless, high beta, supercritical, quasi-perpendicular shock wave. I. Rankine-Hugoniot geometry, currents, and stationarity. *J. Geophys. Res*. **91**, 11019–11052.

SEE, V., CAMERON, R.F. & SCHWARTZ, S.J. 2013 Non-adiabatic electron behaviour due to short-scale electric field structures at collisionless shock waves. *Ann. Geophys*. **31**, 639–646.

THOMSEN, M., STANSBERRY, J., BAME, S. & GOSLING, J. 1987 Strong electron heating at the earth's bow shock. *J. Geophys. Res*. **92**, 10119–10124.

TORBERT, R.B., RUSSELL, C.T., MAGNES, W., ERGUN, R.E., LINDQVIST, P.A., LE CONTEL, O., VAITH, H., MACRI, J., MYERS, S., RAU, D., *et al.* 2016 The FIELDS instrument suite on MMS: scientific objectives, measurements, and data products. *Space Sci. Rev*. **199**, 105–135.

TRAN, A. & SIRONI, L. 2020 Electron heating in perpendicular low-beta shocks. *Astrophys. J*. **900**, L36.

TROTTA, D. & BURGESS, D. 2019 Electron acceleration at quasi-perpendicular shocks in sub- and supercritical regimes: 2D and 3D simulations. *Mon. Not. R. Astron. Soc*. **482**, 1154–1162.

VASKO, I.Y., MOZER, F.S., BALE, S.D. & ARTEMYEV, A.V. 2022 Ion-acoustic waves in a quasi-perpendicular earth's bow shock. *Geophys. Res. Lett*. **49**.

VASKO, I.Y., MOZER, F.S., KRASNOSELSKIKH, V.V., ARTEMYEV, A.V., AGAPITOV, O.V., BALE, S.D., AVANOV, L., ERGUN, R., GILES, B., LINDQVIST, P.A., *et al.* 2018 Solitary waves across supercritical quasi-perpendicular shocks. *Geophys. Res. Lett*. **45**, 5809–5817.

VASKO, I.Y., WANG, R., MOZER, F.S., BALE, S.D. & ARTEMYEV, A.V. 2020 On the nature and origin of bipolar electrostatic structures in the earth's bow shock. *Front. Phys*. **8**, 156.

VINK, J. 2012 Supernova remnants: the X-ray perspective. *Astron. Astrophys. Rev*. **20**, 49–120.

VINK, J., BROERSEN, S., BYKOV, A. & GABICI, S. 2015 On the electron-ion temperature ratio established by collisionless shocks. *Astron. Astrophys*. **579**, A13.

WALKER, S., ALLEYNE, H., BALIKHIN, M., ANDRÉ, M. & HORBURY, T. 2004 Electric field scales at quasi-perpendicular shocks. *Ann. Geophys*. **22**, 2291–2300.

WANG, R., VASKO, I.Y., ARTEMYEV, A.V., HOLLEY, L.C., KAMALETDINOV, S.R., LOTEKAR, A. & MOZER, F.S. 2022 Multisatellite observations of ion holes in the earth's plasma sheet. *Geophys. Res. Lett*. **49**.

WANG, R., VASKO, I.Y., MOZER, F.S., BALE, S.D., ARTEMYEV, A.V., BONNELL, J.W., ERGUN, R., GILES, B., LINDQVIST, P.A., RUSSELL, C.T., *et al.* 2020 Electrostatic turbulence and debye-scale structures in collisionless shocks. *Astrophys. J. Lett*. **889**, L9.

WANG, R., VASKO, I.Y., MOZER, F.S., BALE, S.D., KUZICHEV, I.V., ARTEMYEV, A.V., STEINVALL, K., ERGUN, R., GILES, B., KHOTYAINTSEV, Y., *et al.* 2021 Electrostatic solitary waves in the earth's bow shock: nature, properties, lifetimes, and origin. *J. Geophys. Res* **126**, e2021JA029357.

WILSON, L.B., SIBECK, D.G., BRENEMAN, A.W., CONTEL, O.L., CULLY, C., TURNER, D.L., ANGELOPOULOS, V. & MALASPINA, D.M. 2014*a* Quantified energy dissipation rates in the terrestrial bow shock. 1. Analysis techniques and methodology. *J. Geophys. Res*. **119**, 6455–6474.

WILSON III, L.B., CATTELL, C.A., KELLOGG, P.J., GOETZ, K., KERSTEN, K., KASPER, J.C., SZABO, A. & WILBER, M. 2010 Large-amplitude electrostatic waves observed at a supercritical interplanetary shock. *J. Geophys. Res*. **115**, A12104.

WILSON III, L.B., SIBECK, D.G., BRENEMAN, A.W., CONTEL, O.L., CULLY, C., TURNER, D.L., ANGELOPOULOS, V. & MALASPINA, D.M. 2014*b* Quantified energy dissipation rates in the terrestrial bow shock. 2. Waves and dissipation. *J. Geophys. Res*. **119**, 6475–6495.

WU, C.S. 1984 A fast Fermi process - Energetic electrons accelerated by a nearly perpendicular bow shock. *J. Geophys. Res*. **89**, 8857–8862.

WYGANT, J.R., BENSADOUN, M. & MOZER, F.S. 1987 Electric field measurements at subcritical, oblique bow shock crossings. *J. Geophys. Res*. **92**, 11109.

https://doi.org/10.1017/S0022377824001223 Published online by Cambridge University Press